ORIGINAL PAPER

Design and optimization of polyvinyl-nitride rubber for tensile strength analysis

Sudheer D. Kulkarni[1,2] · Manjunatha[3] · U. Chandrasekhar[4] · K. V. Manjunath[5] · C. Durga Prasad[6] · Hitesh Vasudev[7]

Abstract

In view of its combination of distinctive qualities, including strong tensile and tearing strength along with exceptional dynamic capabilities, which make it a strategic and irreplaceable material to produce bigger tyres, rubber is among the most used polymer in the world. The most widely employed sealing material in mechanical components is rubber. Failing of the rubber sealing in structural parts that seal could result in disastrous mishaps. Rubber seals serve to eliminate scratches brought on by direct contact between the piston and the cylinder block's inner walls and stop the flow of hydraulic oil. Due to the challenging work environment and discomfort of replacing rubber, it is important to suggest greater standards for its dependability. The rubber's reliability may be impacted by several variables over its life cycle, including load fluctuations, environmental factors, and heat treatment. In the current study, polyvinyl-nitrile rubber was subjected to heat treatment. The heat treatment was conducted with varying four different parameters such as curing time, curing temperature, post curing temperature, and post curing time. Based on these four parameters, sixteen samples were heat-treated. The microhardness, tensile properties, and fracture behavior of the tensile samples were analyzed by using Vicker's microhardness tester, universal testing machine, and scanning electron microscope. The outcomes revealed that the curing temperature and curing time has a significant effect on the hardness and tensile properties, and the samples' strength increased by 25% for curing temperature of 170 °C. The fracture analysis revealed that the minimal variation in the fractured micrographs was seen during the heat-treated cycle, showing that the environment seems to have less impact on the rubber matrix's ability to adhere.

1 Introduction

A seal is a tool or a piece of material that effectively shuts an aperture to prevent the entry or exit of air, liquid, or other substances. Since seals are a necessary component of practically all machinery and engines, they have a wide range of industrial applications. Sealing is a need because most process equipment, machinery, and engines work with some sort of fluid. There are many ways to seal a system; hence there are many different types of seals available and created for specific applications. Elastomer seals are generally manufactured using materials such as PVC-Acrylonitrile-Butadiene Rubber (PVC-NBR), Carboxylated Nitrile (XNBR), Ethylene Acrylate (AEM), Ethylene Propylene Rubber (EPR),

✉ Sudheer D. Kulkarni
  sudhir@msrit.edu

✉ C. Durga Prasad
  durgaprasi71@gmail.com

  Manjunatha
  manjunatha.princi@gmail.com

  U. Chandrasekhar
  rapidchandra@gmail.com

1 New Horizon College of Engineering, Visvesvaraya Technological University, Bengaluru, India

2 Department of Industrial Engineering and Management, Ramaiah Institute of Technology, Bengaluru 560054, India

3 New Horizon College of Engineering, Bengaluru, India

4 AddWize-Wipro 3D, Bengaluru 560058, India

5 Siddaganga Institute of Technology, Tumakuru, Karnataka 572104, India

6 RV Institute of Technology and Management, Bengaluru, Karnataka 560076, India

7 Lovely Professional University, Phagwara, India

Ethylene Propylene-Diene Rubber (EPDM), Butyl Rubber (IIR), Choloropropene rubber (CR), Fluorocarbon (FKM), etc. The experimental analysis of the impact of process parameters on a few key characteristics of a few widely used industrial seals is covered by the current work. The following headings feature discussions of the precise goals, the process to be used to achieve them, and potential results.

The literature review covering the use of several seal types in diverse industrial applications was done. Below is a survey of some of the most important and pertinent scientific studies. A brush seal's visualization and characterization process revealed typical locations with diverse sorts of flows. Pressure maps have been made after the axial pressure patterns were determined across various inlet pressure scenarios [1]. Investigations were conducted into how to brush location, geometry, and morphology affected the interaction between the seal surfaces, hydraulic leak, and the resulting pressure decrease [2]. To view and characterize the intricate fluid flow in replicated single and double-brush sealings, a method has been created. Within the brush, the flow patterns and associated fluid speeds have been non-intrusively identified and visually recreated [3]. They used the full-flow field monitoring technique to examine the fluid velocity and flow patterns within a set of brushes. These were graphically reconstructed in order to identify the variables influencing changes in seal leakage [4]. Under stable and lower rotor velocity circumstances, the leak behavior of a brushed sealing with gas fluids has been examined. The given state concept was used as a way of acquiring the statistics for air and CO_2. The results for helium, in contrast to that for air as well as CO, exhibited a distinct curve [5]. For air turbine openers, a non-contacting or clearing seal design made up of several centrifugal blower motors as well as oil-air separators has been created. A prediction of reliability improvement resulting from the development and qualification of a clearing seal to replace a contact driveshaft seal is provided [6].

It explained how to construct, analyze, and evaluate non-contacting gaseous facing sealing for aircraft applications. It has been demonstrated that non-contacting sealing technologies are used in place of contact-facing gaskets in aircraft sealing solutions to increase safety and improve leak variance [7]. Comparing the flow properties of the modeling seals with motor sealing, a non-dimensional resemblance has been found. The brushed sealing pack's homogeneous asymmetric impedance provided adequate flow rate properties. The simulation, nevertheless, did not accurately depict the force distribution patterns [8]. For brushed sealings utilized in aircraft engines, modeling and assessment of brush deformations, bending stresses, and bristle or rotor contacting pressures were performed. These pressures are produced at the interaction of the fiber and rotor surfaces owing to radial fluid flows. The complementing non-dimensional loading relationships have been created. The assessment of brush stresses as well as deformations in the context of brushed sealing mechanical investigation, justifies the application of non-linear beam theory. The location and amount of the high bending stresses have been measured [9]. There was a discussion of the benefits of non-metallic brushed sealings for oiled sealing purposes. In comparison to metallic brushed sealings and labyrinthine sealings, non-metallic brushed sealing leaking effectiveness has been shown to be superior. The advantages of creating the very same have been emphasized [10]. A method for load calculations using a poroelastic method has been created. The brushed sealing was effectively reflected by the findings as a permeable medium with a thin technique [11]. The behavior of the bristle in brushed sealings in 3D space has been predicted using a novel approach and computer programming. The outcomes demonstrated the anticipated behavior of bends seen in live brushed sealings [12]. It has been suggested to create a seal with a design like a brushed sealing but with thin strips in place of the wires seen in typically brushed sealing. This sealing design has been determined to be suitable for use in practice [13]. The rigidity and damping properties of rubber O-rings exposed to little amplitude reciprocating motion can be measured using a test method that has been provided. This might be used to examine a variety of important variables that have an impact on the dynamic characteristics of O-rings [14]. Several researchers tested O-rings under accelerated aging conditions to ascertain how variable their characteristics were. Some researchers treated the compression set as a single parameter. It was discovered that the NBR O-ring in an electro-hydraulic mechanical actuation age considerably more slowly than one that is solely exposed to air. It was challenging to estimate the lifetime of O-rings due to a lack of failure data. Thus, the accelerated deterioration test has been employed by numerous researchers to determine the O-rings' expected lifetime [15, 16]. To comprehend the impact of working conditions on the qualities of the seals, accelerated thermal aging studies on nitrile rubber O-rings were carried out [17, 18]. A study was conducted to look into the usage of an alternative material for the rectangular groove-encased fluorocarbon seal in nuclear fuel delivery flasks. The permeability to liquid, hydrogen, calcium, or magnesium salt solution and radiation resistance were considered while comparing the present seal materials to EPDM sealings. The results showed that the EPDM polymers performed well in terms of mechanical characteristics, radiation resistance, and moisture resistance. Gas and water were discovered to have greater permeation rates [19]. The effect of aging on the ability of elastomeric O-rings to seal was studied, and it was discovered that the leakage rate decreased with aging. A significant decline in other material properties, however, demonstrated that component functions like static leakage rate do not always correlate with other mechanical properties

[20]. According to investigations [21, 22], rubber O-ring sealings assist in preventing scratches generated by immediate communication between the piston and the cylinder block's inner wall, as well as the leaking of hydraulic fluid. O-ring utilization is restricted by factors including extreme temperatures, rapid rubbing motions, hostile environments for elastomeric materials, cylinder ports that seals must cross, and wide shaft clearances [23]. O-ring sealings, an example of an elastomer sealing, are used extensively throughout many industry sectors for a variety of reasons, including their broad operational range, ease of maintenance, low risk of causing structural damage, compact design, high likelihood of reusability, gradual failure, low cost, etc. [24]. Utilizing fracture mechanics, the rupture behavior of rubbers was analyzed. For non-crystallizing rubbers, it was noted that there was a good correlation with the experiment. However, under these test conditions, crystallization cannot take place for natural rubbers that are strain crystallizing [25]. The responses that were chosen for rubber material utilized in footwear soles were elongation at break and slip resistance. Particle swarm optimization and backpropagation neural networks were the two optimization methods used. To achieve greater elongation and slide resistance, mold temperature, mold pressure, and holding time were optimized. There was a 30% decrease in the cost of quality, according to experimental validation data [26, 27].

The comparison was made between two distinct calibration methods of monitoring ozone content. The German rubber business refers to a wet chemical analysis procedure, while the international rubber industry uses UV spectroscopy. These two approaches would produce various outcomes. Investigating the outcomes of real-world ozone testing using samples of rubber was done side by side. Discussions were held regarding the effects of the variances in the ozone concentration estimates produced by the two calibration techniques [28].

Properties of rubber compound used in industrial seals were studied and a relation predicting the properties for varied manufacturing parameters was established using machine learning techniques [29]. Compression set and shear strengths were compared by varying the processing conditions of a rubber compound widely used in sealing applications [30].

From the literature review, the following components have been identified. One of the crucial components of any machine or engine is the sealing, and the effectiveness of the seal has a big impact on how well the system works. To optimize the process parameters used in the manufacture of seals, extensive research is being conducted. Tensile strength tests and microhardness tests are the most frequent tests performed on elastomer seal materials. Fracture analysis could be explored to study the failure process.
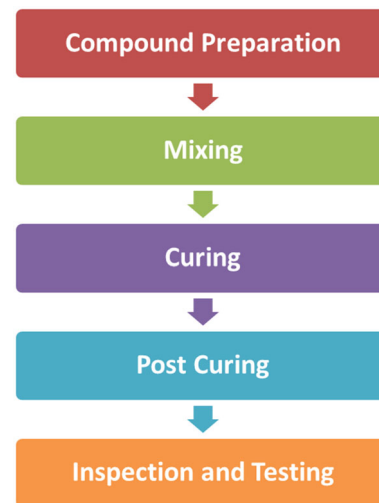

Fig. 1 Process flow chart of elastomer seal manufacturing process

2 Experimental description

2.1 Processing

The process flow chart of the elastomer seal manufacturing process is shown in Fig. 1. In order to create NBR, acrylonitrile (CH2=CHCN) and butadiene (CH2=CH–CH=CH2) must first be emulsified in water before their single-unit molecules can be joined together to form larger, multi-unit molecules under the influence of free-radical initiators. Between 15 and 50 percent of the finished copolymer contains acrylonitrile. The rubber gets stronger, more resistant to swelling by hydrocarbon oils, and less permeable to gases as its acrylonitrile content rises. However, due to the greater glass transition temperature of polyacrylonitrile, the rubber loses flexibility at lower temperatures (i.e., the temperature below which the molecules are locked into a rigid, glassy state). The following key components were added to the compound in parts per hundred rubbers (phr). NBR = 70, PVC = 30, Dioctyl Phthalate (DOP) = 50, with trace amounts of Zn Stearate, Zn Oxide, Stearic Acid, and Sulfur as a compatibilizer.

On observing the process and discussing it with the process engineers, it was understood that curing and heat treatment processes were ideal to be considered for this study as they consumed significant time and energy resources. The cause-and-effect diagram is constructed to understand the factors affecting the response variables. Figure 2 shows the cause-and-effect diagram with reference to the mechanical properties of the PVC-NBR constructed using the R software package.

To determine the ideal values of the parameters affecting the mechanical properties of the O-rings, the experiment used a 2^4-design with three replicates. The experiment run order

Fig. 2 Cause-and-effect diagram
for mechanical properties
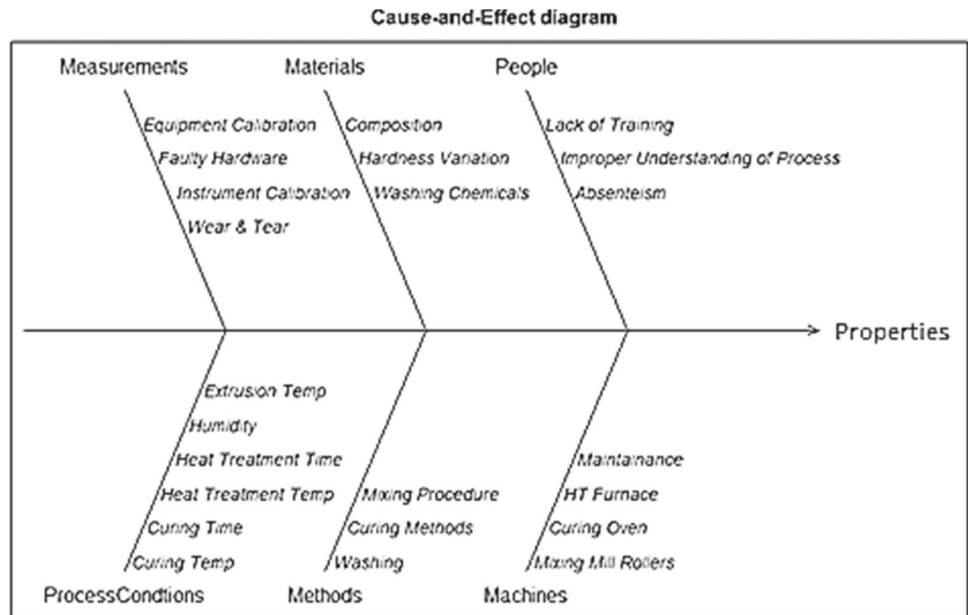
was generated using Minitab software. Manufacturing process control parameters, namely, curing temperature (150 °C, 170 °C), curing time (14 min and 18 min), post curing temperature (50 °C and 100 °C) and post curing time (60 min and 120 min) were varied and the response variables considered were tensile strength, load at the break, and percentage elongation.

Pilot runs were conducted to ensure the proper functioning of the equipment. The process was carefully monitored to ensure that everything was done according to the plan. It was taken care to set the parameters as per the experimental design. Standard order was formulated considering the process parameters. To eliminate the effect of noise, the order of running the experiment was randomized. The samples were then analyzed for microhardness and tensile properties.

2.2 Property evolution

Shore A Microhardness testing is carried out as per IS 3400 (part-2): 1995 and is conducted to determine the microhardness of the specimens cured and heat treated at various temperatures and duration combinations. The specimens are inspected for any defects and then placed on hard, even, and horizontal surfaces. The tester is held in a vertical position, and pressure is applied evenly until the pressure foot makes firm contact with the specimen surface. The upper and lower surfaces of the test piece should be lightly dusted with talcum powder. The indenter of the microhardness tester is placed on the flat surface of the test piece for at least 5 s, and the reading is taken. Readings are taken; at either 3 to 5 different points distributed over the test piece, and the average value is calculated.

The tensile samples were prepared as per the ASTM-E8 standards. The die is left to pre-heat to the necessary temperature, which is 150 °C or 170 °C. The mixing stage produces 73–75 g of rubber compound, which is then collected. After the mold has heated up, the die is opened and filled with rubber compound. 150 kg/cm^2 of pressure and 14 or 18 min of cure time are the settings. To guarantee consistent material distribution, the die is put into the pressing machine and bumped twice. The timer has been set. The sheet is removed from the die after it has been allowed to cure for the allotted amount of time. To get rid of the excessive glare, the sheet is cut. To ensure adequate proportions and a nice surface, the sheet is examined. After that, it can cool. The cooled sheet is installed on a hydraulic press and then cut into tensile test specimens in the shape of Dumbles. The specimen's length and thickness are measured. The tensile test was carried out on a universal testing machine with a crosshead speed of 0.25 mm/min. The accepted specimen is next brought to the tensile testing equipment for examination. The tensile specimens are shown in Fig. 3.

3 Results and discussion

3.1 Mechanical properties

The tensile test is carried out as per IS 3400 (Part-1):1987 Standards. The dumbbell-shaped test specimen is prepared as described above, and a length of 25 mm is marked in the span region. It is mounted on the tensile testing machine onto the roller gripper attachments. It is ensured that the test piece is held firmly by both the top and bottom grippers uniformly.

Fig. 3 Photograph of tensile test specimen

The specimen mounting is checked for perpendicularity with the gripper. A new file is opened in the testing software is opened. All the data with respect to workpiece dimensions, specimen number, material, etc., are entered. Load cell numbers (1, 2, 3) and test units (kg, kN, N) are selected as per the requirements. The group name can be added if required. On clicking next, the testing window is displayed. This window displays three different partitions, namely the graphs of Load versus Elongation, Stress versus Strain, and Load versus Time. Parameters such as length, width, thickness of the specimen, and test speed are entered. The sample set-up is completed. On clicking Start, the machine applies a tensile load on the specimen. The machine stops automatically after the specimen breaks. All the results are displayed on the monitor. The report can be generated by clicking the 'Report' button, and the report print preview can be viewed.

Combinations of curing temperature, curing duration, post curing temperature, and post curing time were designed and tested for tensile strength investigation. The tensile properties are shown in Table 1.

The tensile strength of Sample-1 is 6.59 N/mm^2, it was slightly increased to a value of 6.67 N/mm^2 for Sample-2, and showed significant increase to 7.44 N/mm^2 for Sample-3. The tensile strength was decreased further to a value of 7.25 N/mm^2 for Sample-4 due to an increase in post curing temperature, increased to a value of 7.73 N/mm^2 and 8.17 N/mm^2 for Sample-5 and 6 due to an increase in curing time. Finally, the tensile strength value increased to a value of 7.8375 N/mm^2 due to an increase in post curing time. Overall, the highest and lowest tensile properties were recorded for Sample-5 and Sample-1.

The response variables for this experiment were percentage elongation, modulus at 100%, and tensile strength. The experiment was run in a random order to reduce the impact of noise. Each experiment was chosen at random. Run and

standard orders were determined. Plots of the main effects and interaction effects were made using Minitab software. Tensile strength's effects are shown in Fig. 4, while its interaction is shown in Fig. 5.

Understanding how the specimen fails and how the crack travels from the outside layer to the inner layer is made easier by the experimental data set. This event is described in more detail in the part that comes next. The main effects plots for tensile strength shown in Fig. 4 reveals that curing temperature of 150 °C, curing time of 14 min, post curing temperature of 50 °C and post curing time of 120 min give an effect on improvement of tensile strength. Curing time and curing temperature have a significant impact on the tensile strength as inferred from interaction plots portrayed in Fig. 5**.**

Analysis of Variance (ANOVA) was conducted for tensile strength to know the significant factors influencing the results. It observed from Fig. 6 that the P value for curing temperature and combination of curing time-heat treatment time is low; hence they play a significant role in controlling the tensile strength. The R^2 value is found to be high, which indicates that the data best fits the model. Curing time and heat treatment time also play a role in controlling the tensile properties.

The following combinations of curing temperature, curing duration, post curing temperature, and post curing time were tested for Shore A microhardness. Table 2 presents the microhardness results.

The microhardness of Specimen-1 is 69 HV, it was increased to 71 HV for Specimen-2 due to the increase in post curing time, and the microhardness was decreased to 68HV for Specimen-3 owing to the decrease of post curing temperature and post curing time. The same microhardness (i.e., 68 HV) was maintained for Sample-4; it was increased to 70 HV for Sample-5 due to the increase in post curing time, and the same microhardness was maintained for Sample-6. The microhardness was decreased slightly to a value of 69 HV for Sample-7 because of a decrease in post curing temperature and post curing time, increased to 71 HV for Sample-8 due to an increase of the post curing time, again increased slightly to a value of 72 HV for Sample-9 due to increase of post curing temperature, and the same microhardness (i.e., 72 HV) was maintained for Sample-10. The microhardness then decreased to a value of 70 HV for Sample-11 due to a decrease in post curing temperature and post curing time, decreased slightly to a value of 69 HV, and the same microhardness (i.e., 69 HV) for Sample-12, Sample-13, and Sample-14. Finally, the microhardness slightly decreased to a value of 68 HV for Sample-15 due to a decrease in the post curing time, and the same microhardness remained same for Sample-16.

Overall, by analyzing Figs. 7, 8 and 9, which illustrate the main effects, interactions plots and ANOVA for hardness, it has been found that the material's microhardness has grown

Table 1 Tensile test results

Std. order	Run order	Extension (mm)	Displacement (mm)	Yield load (N)	Tensile strength (N/mm²)
7	1	55.40	130.30	85.222	7.10
9	2	55.60	129.10	87.478	7.29
3	3	54.20	130.30	89.243	7.44
5	4	58.30	135.40	98.07	8.17
15	5	49.60	124.00	87.87	7.32
6	6	60.00	132.90	92.774	7.73
10	7	59.30	134.10	94.049	7.84
13	8	44.20	115.80	84.34	7.03
12	9	45.30	113.90	86.988	7.22
8	10	62.30	139.20	85.222	7.10
14	11	54.40	124.00	91.401	7.62
16	12	54.80	118.90	85.713	7.14
11	13	51.20	121.50	97.187	8.10
4	14	53.30	130.30	86.988	7.25
2	15	45.70	113.90	80.025	6.67
1	16	45.90	112.60	79.142	6.59

Fig. 4 Plots of main effects for tensile strength
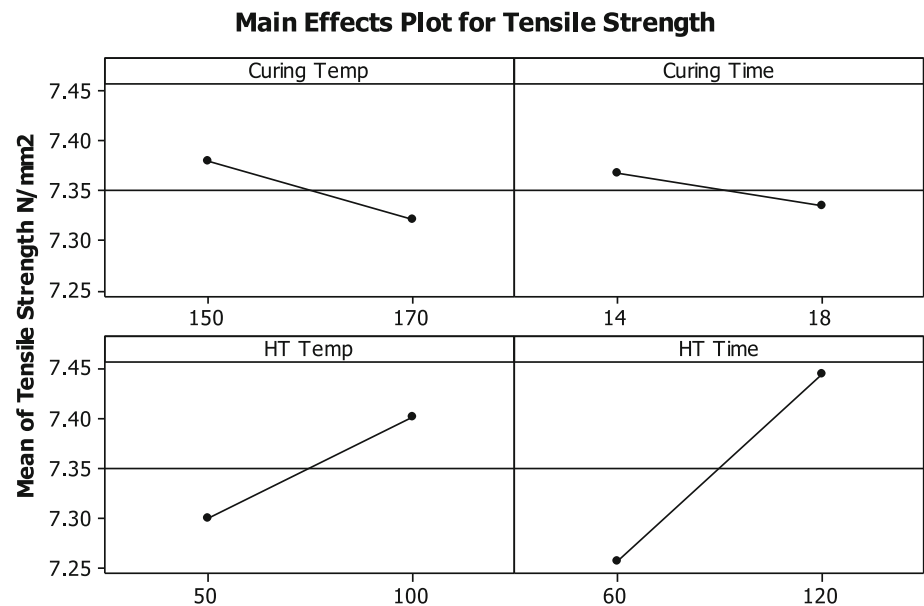
as the curing temperature has risen. The microhardness number varies by no more than 2, with a maximum of 72 and a minimum of 68. It is also clear that post curing has little effect on specimens 9 and 10 because the microhardness number is unaffected by post curing times of 60 and 120 s.

The tensile investigations of these portions were conducted under identical circumstances by Rattapol et al. [31]. In order to remove the impact of outside influences on the test and guarantee the precision of the comparison test. Findings from the tensile tests of 16 specimens with varying porosities that had not undergone heat treatment have been contrasted

with those of the corresponding heat-treated samples. The ultimate strength of the heat-treated sample has been typically higher compared to the un-treated sample when both specimens were identical in permeability. The heat-treated sample had a smooth first linear elastic tension phase and a sharper slope. Additionally, the heat-treated specimen's strength was improved substantially. The cause of this phenomenon is that heat treatment releases the mechanical power (frictional elastic potential) created by the cold pressing of the wire and partially removes the residual stress in the specimen
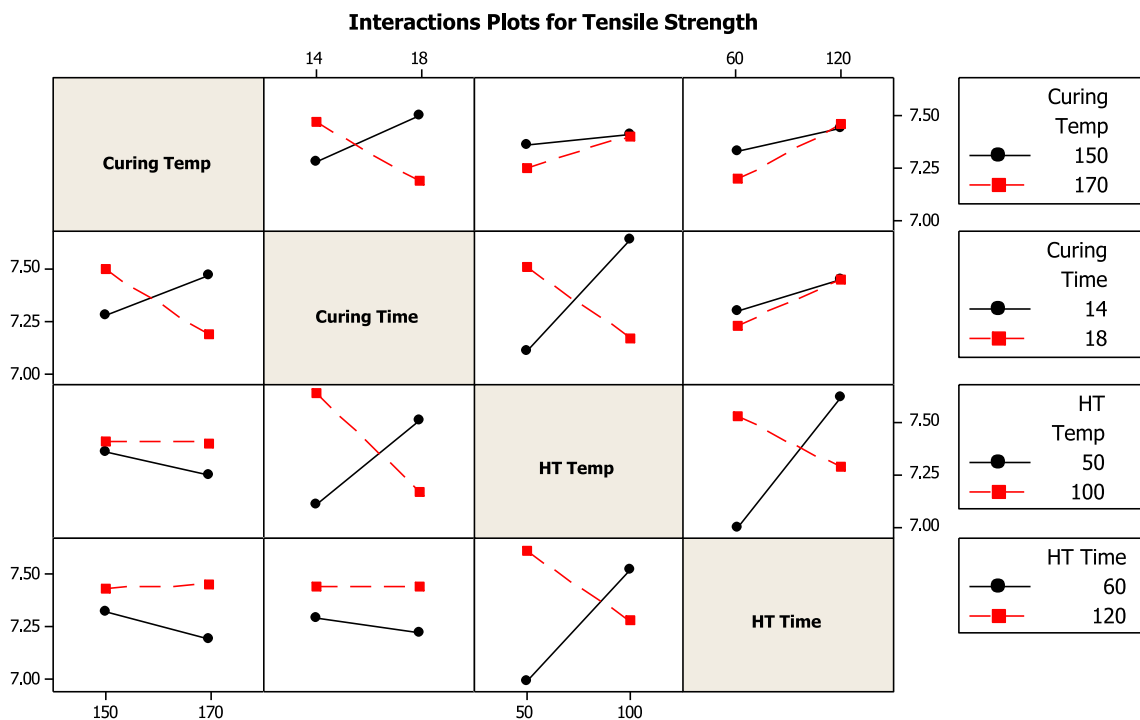
Fig. 5 Interaction plots for tensile strength

```
MANOVA for Curing Temp                           MANOVA for HT Temp
s = 1    m = -0.5    n = 4.5                      s = 1    m = -0.5    n = 4.5

                  Test         DF                                   Test         DF
Criterion         Statistic    F    Num  Denom    P    Criterion    Statistic    F      Num  Denom    P
Wilks'            0.97000  0.340    1     11  0.571    Wilks'       0.92089  0.945      1     11  0.352
Lawley-Hotelling  0.03093  0.340    1     11  0.571    Lawley-Hotelling 0.08591 0.945   1     11  0.352
Pillai's          0.03000  0.340    1     11  0.571    Pillai's     0.07911  0.945      1     11  0.352
Roy's             0.03093                             Roy's         0.08591


MANOVA for Curing Time                           MANOVA for HT Time
s = 1    m = -0.5    n = 4.5                      s = 1    m = -0.5    n = 4.5

                  Test         DF                                   Test         DF
Criterion         Statistic    F    Num  Denom    P    Criterion    Statistic    F      Num  Denom    P
Wilks'            0.70631  4.574    1     11  0.056    Wilks'       0.99658  0.038      1     11  0.849
Lawley-Hotelling  0.41581  4.574    1     11  0.056    Lawley-Hotelling 0.00344 0.038   1     11  0.849
Pillai's          0.29369  4.574    1     11  0.056    Pillai's     0.00342  0.038      1     11  0.849
Roy's             0.41581                             Roy's         0.00344
```

Fig. 6 ANOVA for tensile strength with varying process parameters

that was caused by the pretreatment and higher temperature treatments. Within a particular range of permeability, the ultimate strength of the test specimen steadily dropped as permeability increased. It was the case since the samples with high permeability included less metallic wires and had been, therefore, unable to tolerate greater tension forces, whereas the test sample's elasticity rose as permeability rose. This has been caused by the weaker connections between the spiral wires and the wires during the drawing process in the sample with greater porosity. As an outcome, it was simpler to straighten them, which increased elongation progressively. They concluded that both heat-treated and un-treated specimens' tensile qualities declined as permeability increased, as well as the heat-treated specimens generally had greater tensile characteristics than the un-treated samples. This could be explained by the observation that there are unique variations in the test specimen's inner structure upon processing, which cause a tiny variance in the tensile results. Additionally, on one side, the heat treatment would deteriorate the test specimen's internal component and its mechanical qualities.

Table 2 Hardness number for varying curing parameters

Sp. No.	Curing temp. °C	Curing time, Min	Post curing temp. °C	Post curing time, Min	Hardness (VHN)
1	150	14	100	60	69
2	150	14	100	120	71
3	150	14	50	60	68
4	150	14	50	120	68
5	150	18	100	60	70
6	150	18	100	120	70
7	150	18	50	60	69
8	150	18	50	120	71
9	170	14	100	60	72
10	170	14	100	120	72
11	170	14	50	60	70
12	170	14	50	120	69
13	170	18	100	60	69
14	170	18	100	120	69
15	170	18	50	60	68
16	170	18	50	120	68

Fig. 7 Main effects plots for hardness
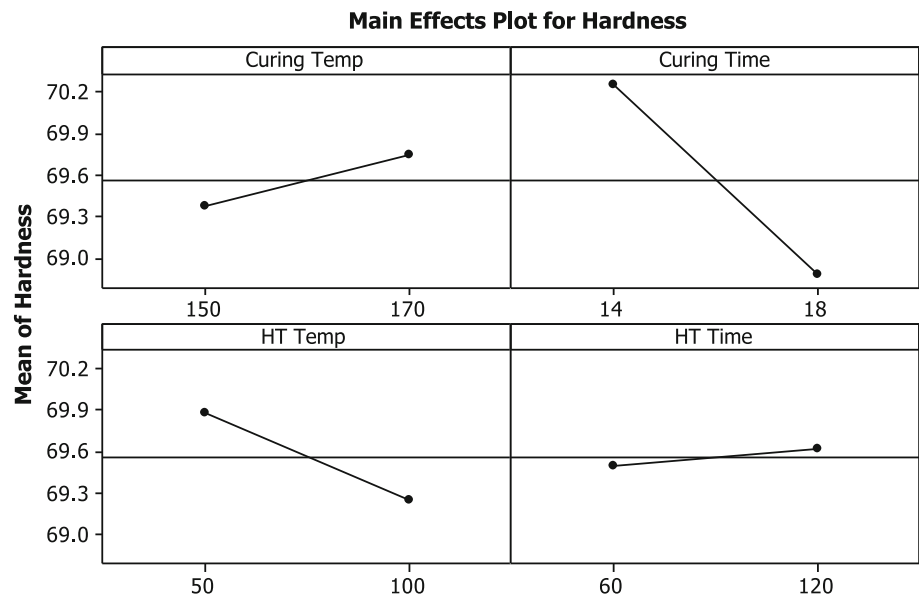
On the other side, in the tensile testing, the tensile fixtures would lose a little bit of force when retaining the specimen for structural purposes and this will affect the accuracy rate of the apparatus directly.

The mean tensile performance of each specimen is documented findings by Calrke and Chough [32, 33]. Their results demonstrate how well the carbon black has an impact on each specimen set's tensile strength. Furthermore, polyblend specimens showed greater tensile strengths than un-filled vulcanized rubber specimens. This discovery might be explained by effective rubber-filler interaction. Although un-cured rubber and carbon black initially mixed effectively, rubber chains have a chance of coming into touch with the material and becoming twisted or caught in the gaps of carbon black aggregate. Rubber chains that have been entwined on the surface of the carbon black granules served as physical cross-links. Physical cross-linking prevents rubber chains from moving around and prevents the rubber from deforming, enhancing the ML of injected rubber even when it is still in the un-cured stage. The torque is increased when polymer chains
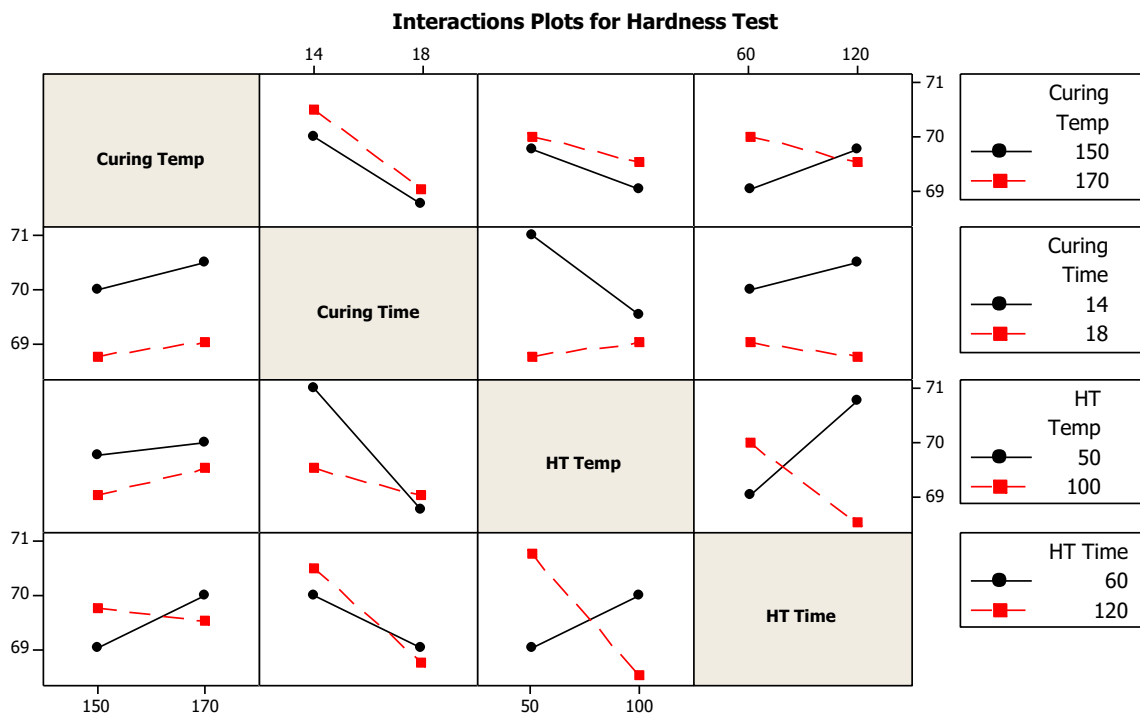
Interactions Plots for Hardness Test

Fig. 8 Interactions plots for hardness

```
MANOVA for Curing Temp                          MANOVA for HT Temp
s = 1    m = -0.5    n = 4.5                     s = 1    m = -0.5    n = 4.5

                  Test              DF                              Test              DF
Criterion       Statistic     F   Num  Denom    P   Criterion     Statistic     F   Num  Denom    P
Wilks'           0.99516   0.053   1    11   0.821  Wilks'         0.98577   0.159   1    11   0.698
Lawley-Hotelling 0.00486   0.053   1    11   0.821  Lawley-Hotelling 0.01443 0.159   1    11   0.698
Pillai's         0.00484   0.053   1    11   0.821  Pillai's       0.01423   0.159   1    11   0.698
Roy's            0.00486                            Roy's          0.01443


MANOVA for Curing Time                          MANOVA for HT Time
s = 1    m = -0.5    n = 4.5                     s = 1    m = -0.5    n = 4.5

                  Test              DF                              Test              DF
Criterion       Statistic     F   Num  Denom    P   Criterion     Statistic     F   Num  Denom    P
Wilks'           0.99840   0.018   1    11   0.897  Wilks'         0.95224   0.552   1    11   0.473
Lawley-Hotelling 0.00160   0.018   1    11   0.897  Lawley-Hotelling 0.05015 0.552   1    11   0.473
Pillai's         0.00160   0.018   1    11   0.897  Pillai's       0.04776   0.552   1    11   0.473
Roy's            0.00160                            Roy's          0.05015
```

Fig. 9 ANOVA for hardness with varying process parameters

are entangled with carbon black, acting as physical cross-links in elastomers. The amount of physical cross-linking is shown by ML, the torque required to melt un-cured rubber at 150 °C. The tensile strength of vulcanized rubber is between 0.5 and 15 MPa, with the polyblend of NBR exhibiting the ultimate tensile strength. Vulcanized rubber substances range in microhardness from 32 to 51, with NBR exhibiting greater microhardness due to the acrylonitrile element in its molecular structure. Generally, reinforcing rubber compounds outperform unfilled vulcanized rubber materials in terms of tensile strength.

3.2 Fracture analysis

The fracture images and tensile fractured images of all the conditions are shown in Figs. 10, 11, 12, and 13. Minimal variation in the fractured micrographs was seen during the heat-treated cycle, showing that the environment seems to have less impact on the rubber matrix's ability to adhere.
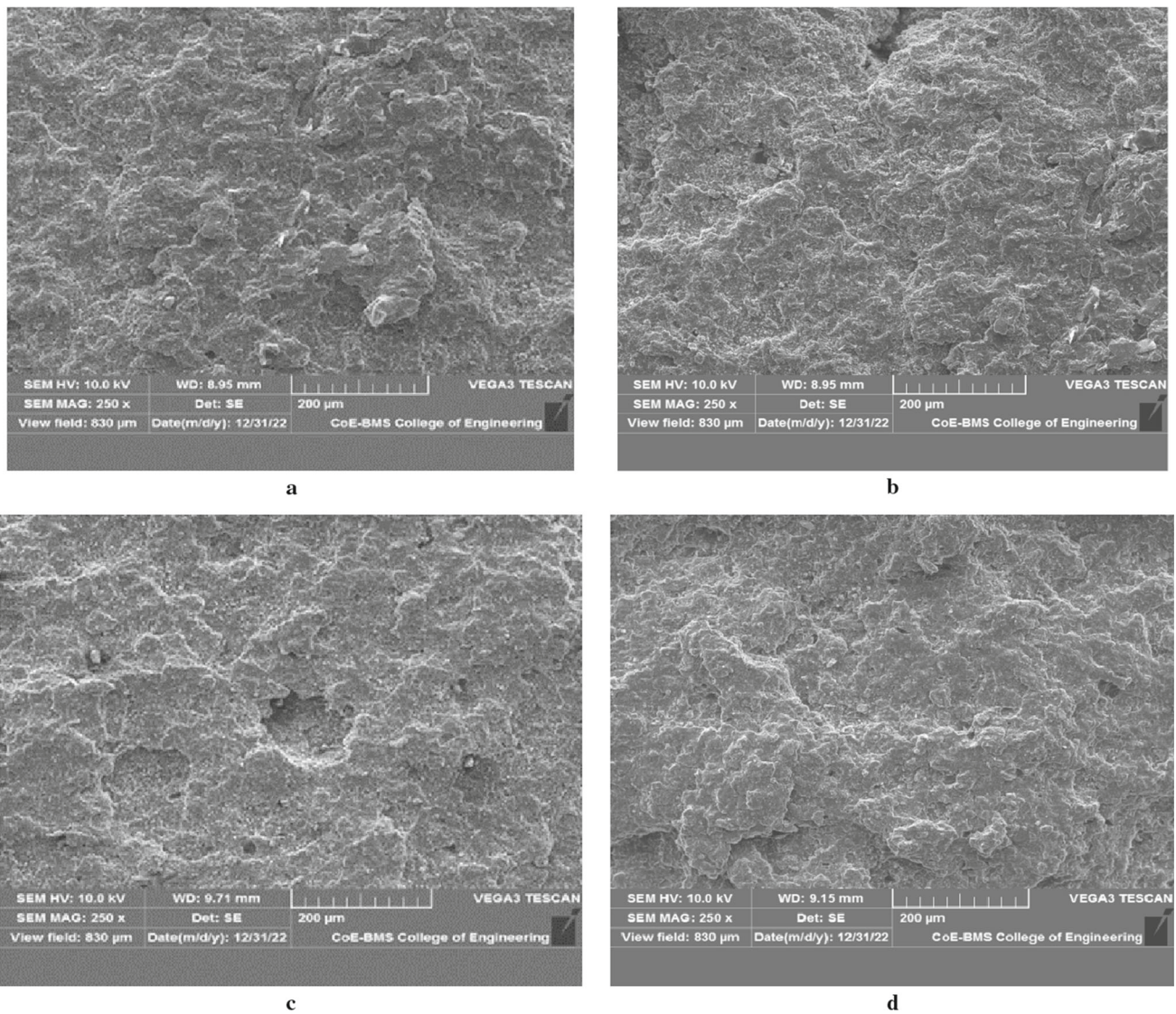
Fig. 10 SEM images of the fractured samples under different conditions (150-14)

Various researchers also studied the fracture behavior of heat-treated rubber. Not that all tears are caused by foreign substance harm. Cracks form as a result of excess tension in vulnerable regions. White et al. [34] used both optical microscopy LOM) and scanning electron microscopy to study an inner rubber fracture. An OM magnification of 20 × has been discovered to be adequate for recording the coarser striation marks. On the other side, scanning electron microscopy has been necessary to reveal the inner fractures caused by fatigue striation marks which have been visible at beaded locations and on one shoulder, as shown in Fig. 10a–d. Additionally, the authors showed how the improved field of view of the scanning electron microscope could be employed to investigate deeper into closed fissures quite effectively than with the OM. Large-scale striation marks on tread separating substrates that are apparent to the naked eye are thought to be growth-arrest patterns, and if correctly examined, they can yield valuable data. The meniscus instabilities across the full width of the spreading rip determine how the striation marks may curve or bend. The striation marks would be bent in the reverse directions from what would happen if the rip had been capable of moving more rapidly along the crown, whether it advances more quickly at the shoulder regions. In the current experiment, the propagation pathway that favored the crown region and the bow direction were congruent. The rubber sections can sometimes disclose regions of permeability that are typically confined to specific regions, as shown in Fig. 11a–d. The placement of such permeable regions is crucial data that can help explain how they formed. The trapped air kind of blow brought on by too much air in the tyre cable was depicted in a photo by Jenkins et al. [35].
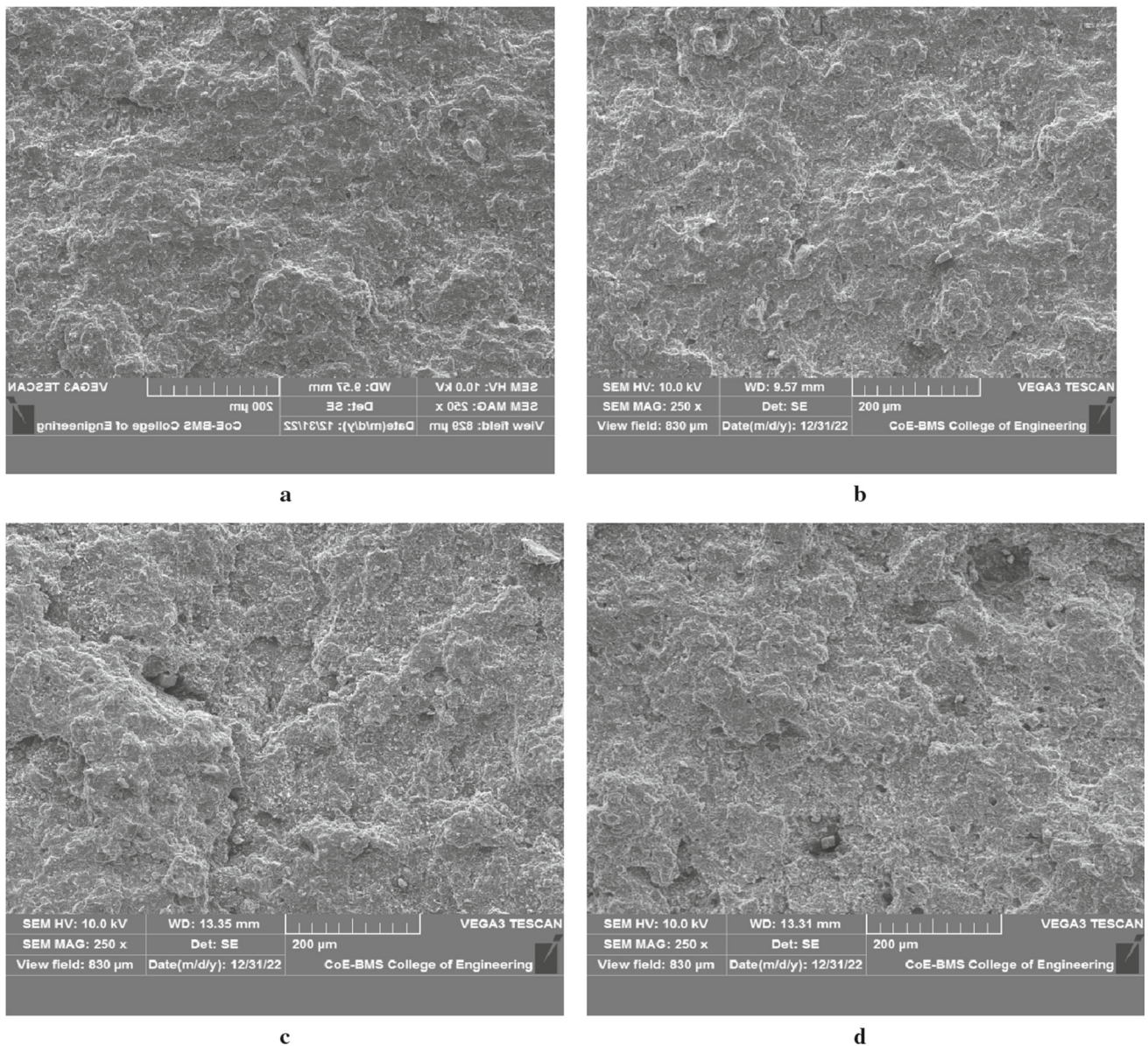
Fig. 11 SEM images of the fractured samples under different conditions (150-18)

A blow occurred between the flanges consequently. Illustration of a strike to the shoulder shows additional pockets of permeability are seen because of extreme heat accumulation [36]. Cell wall investigation under a microscope occasionally produces diagnostic data. Cell walls may have a smooth, smooth yet pock-marked or gritty texture. Because of rubber tear, permeability caused by excess heat accumulation in a "hot spot" while in use frequently exhibits a grainy texture on cell walls. While the source of permeability brought on by early access of pressure after polymerization typically results in cell walls that are mirror-smooth. The presence of blossoming on the cell wall surfaces should also be noted (Fig. 12a–d) because this could reveal further crucial details regarding the porosity's temperature history. The walls of

confined air pockets are mirror-smooth. The scanning electron microscope is especially useful for viewing the surface areas of cells at higher magnifications.

Overload or fatigue-related rubber failures mainly include many components. The inner rubber breakdown has been brought on by rubber fatigue [37–39]. "More mileage would have caused the treads and carcasses to separate." Other findings demonstrated entrapped air and undesirable particles to be the starting point of fatigue damage in samples. The source of blistering in a vehicle tyre sidewall and found that the mechanism that led to the blistering was tension fatigue in rubber starting at the helices of the tyre cables [40–44]. When the early, isolated divisions had gotten, big sufficient,
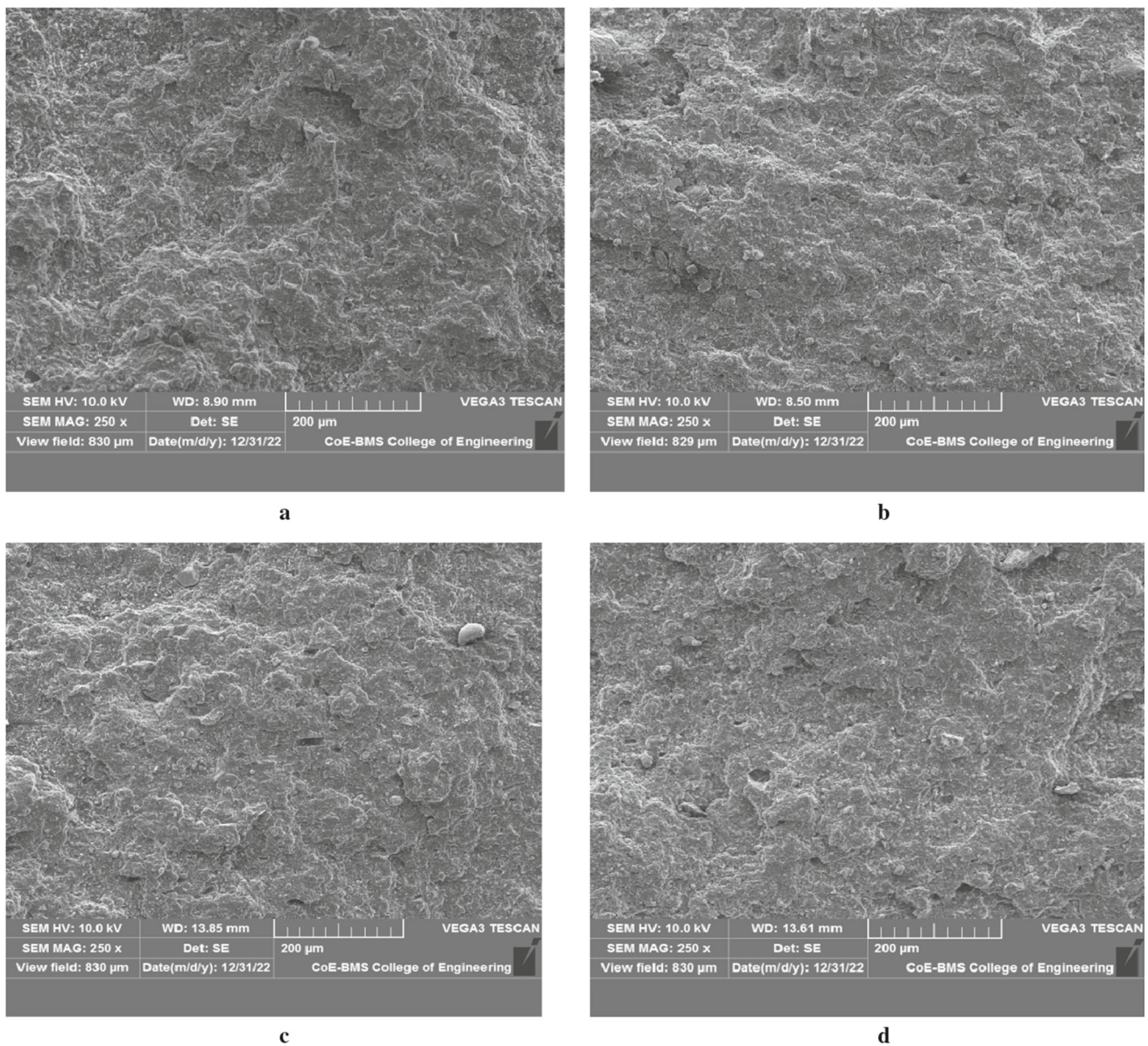
Fig. 12 SEM images of the fractured samples under different conditions (170-14)

cable-to-cable propagation began. When air pressure eventually arrived, it compelled the divide to widen. A scanning electron microscope photograph of a rubber fracture starting at the top of a glass cable utilized as a belt in earlier belted bias vehicle tyres was displayed [45–50]. The additional scanning electron microscope image of the damaged surface exhibited an interface abrasion-rounded texture that was comparable to the texture often associated with carbon black aggregation prominences, as shown in Fig. 13a–d.

A portion of the tyre with microcracks emerging near cable endpoints at the belt edges of a wire-belted vehicle tyre as a photo-micrograph in one of many studies concerned with the beginning and spread of fractures in cable-rubber laminates [51–60]. The belt edge phase separations in-depth and

provided additional micro images displaying the texture of these fissures when they were not covered by interface abrasion, both on tyre carcasses and tread pieces ejected from them. In certain instances, it has been shown that stereoscopic magnifications and crucial lighting can reveal data on the direction of ripping. Surface textures of tears among vehicle tyre belt wires brought on by belt edge separations have also been shown [61–68]. Their findings demonstrate the intricacy of tear topologies, with one resulting from "ring rips" that are packed lengthwise along the wire resembling shish kebabs and another from larger-scale radial tearing that advance across iron belts out from belt edges towards the tire's crown [69–78]. For instance, involving non-rubber part fatigue, methodically examined the fracture ends of Nylon
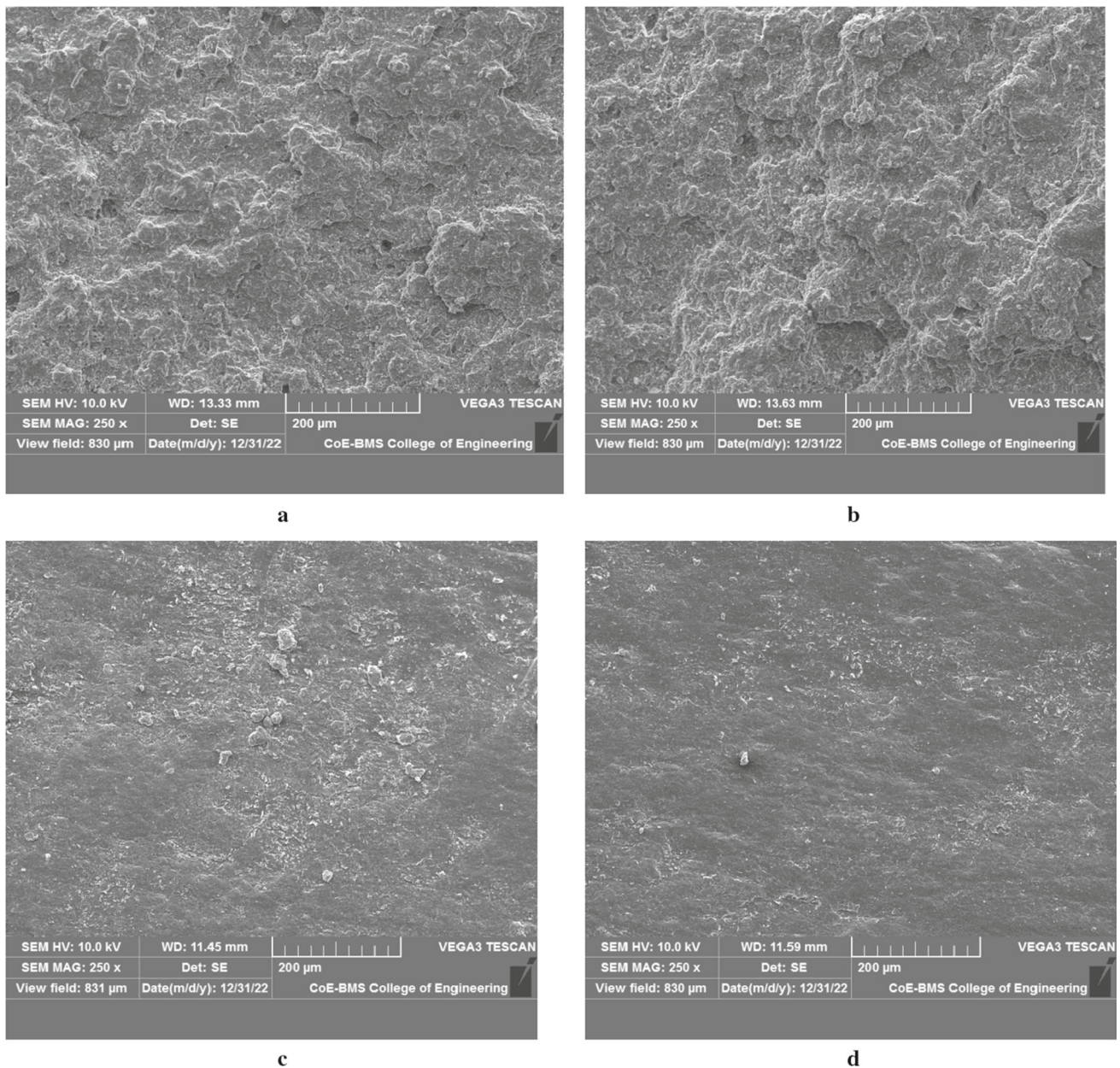
Fig. 13 SEM images of the fractured samples under different conditions (170-18)

tyre cables removed from failing vehicle tyre sidewalls in order to find a solution to the fatigue issue. An investigation under a microscope showed that bias ruptures had caused Nylon threads to break [79–85].

The level of fatigue failure in any one place could be measured by counting skewed shape breakages inside a single cable, and an explanation underlying the occurrence was put forth. It may be inferred from the numerous research and current investigations that this environment can lessen the rubber matrix's adherence. As a result, this environment has an impact on the rubber strength, but that impact is much less pronounced than it is in the heat-treated environment [86–92].

4 Conclusions

In the present study, the polyvinyl rubber was subjected to different heat treatments by varying the processing variables such as curing time, curing temperature, post curing temperature, and post curing time. Then the mechanical characteristics such as microhardness, tensile properties, and fracture behavior were analyzed, and the following conclusions were drawn. The tensile strength increased with the increase in the curing time and curing temperature. The values of load at break are analyzed; it observed that the P value for curing temperature and combination of curing time-heat

treatment time is low; hence they play a significant role in controlling load at the break. The R^2 value is found to be high, which indicates that the data best fits the model. Observations of main effects plots indicate that the mean load at break is high when the curing temperature is high, i.e., 170 °C. Curing time and heat treatment time also play a role in controlling the load at the break. The hardness also followed a similar trend to tensile strength. Overall, it is observed that as the curing temperature increases, the hardness of the material has increased. The variation in the hardness number is within a range of 2, with a maximum of 72 and a minimum of 68. It can also be seen that for specimens 9 and 10, post curing is not playing a significant role, as for post curing of time of 60 and 120, the hardness number remains unaltered. It was concluded from the fracture analysis that the environment could lower the rubber matrix's adherence. As a result, this environment has an influence on rubber strength, but that impact is much less pronounced than it is in the heat-treated environment.

References

1. Braun, M.J., Hendricks, R.C., Canacci, V.: Flow visualization in a simulated brush seal. In: ASME Gas Turbine and Aeroengine Congress Paper ASME 90 GT-217, (1990)
2. Braun, M.J., Hendricks, R.C., Yang, Y.: Effects of brush seal morphology on leakage and pressure drops. In: AIAA/SAE/ASME/ASEE 27th Joint Propulsion Conference, Paper AIAA 91-210, (1991)
3. Braun, M.J., Canacci, V.A., Hendricks, R.C.: Flow visualization and quantitative velocity and pressure measurements in simulated single and double brush seals. Trib. Trans. 70–80 (1991)
4. Braun, M., Canacci, V.: Flow visualization and motion analysis for a series of four sequential brush seals. In: AIAA/SAE/ASME/ASEE 26th Joint Propulsion Conference, Paper AIAA 90-2482 (1992)
5. Carlile, J.A., Hendrics, R.C., Yoder, D.A.: Brush seal leakage performance with gaseous working fluids at static and low rotor speed conditions. ASME J. Eng. Gas Turbines Power **115**, 397–403 (1993)
6. Giesler, W., Mathis, D., Hager, J.: High reliability oil-air high-speed gearbox clearance seal. In: AIAA/SAE/ASME/ASEE 34th Joint Propulsion Conference, Paper AIAA 98-3287, (1998)
7. Menendez, R.P.: Development of lift-off seal technology for air/oil axial sealing applications. In: AIAA/SAE/ASME/ASEE 35th Joint Propulsion Conference, pp. 99–110, (1999)
8. Chen, L.H., Wood, P.E., Jones, T.V., et al.: Detailed experimental studies of flow in large scale brush seal model and a comparison with CFD predictions. Trans. ASME. **122**, 672–679 (2000)
9. Zhao, H., Stango, R.J.: Effect of flow-induced radial load on brush seal/rotor contact mechanics. Trans. ASME. **126**, 208–215 (2004)
10. Nitin Bhate, A.C. Non-metallic brush seals for gas turbine bearings. In: ASME Turbo Expo 2004: Power for Land, Sea and Air, pp. 1–6. ASME. Vienna, (2004)
11. Dogu, Y.: Investigation of brush seal flow characteristics using bulk porous medium approach. Trans. ASME. **127**, 136–143 (2005)
12. Cesare Guardino, J.W.: Numerical simulation of three-dimensional bristle bending in brush seals. J. Eng. Gas Turbines Power **127**, 583–590 (2005)
13. Saber, E., Khaled, M.: Advanced seal design for rotating machinery. Am. J. Sci. Indus. Res. **2**, 58–68 (2011)
14. Green, I., Etsion, I.: Pressure and squeeze effects on the dynamic characteristics of elastomer 0-rings under small reciprocating motion. J. Tribol. **108**, 439–444 (1986)
15. Meeker, W.Q., Escobar, L.A., Lu, C.J.: Accelerated degradation tests: modeling and analysis. Technometrics **40**(2), 89–99 (1999)
16. Mingjun, Z., Jilong, X.: Finite element analysis of large deformation of rubber parts under compression. J. Beijing Jiaotong Univ. **25**, 76–79 (2001)
17. Chupp, R.E., Ghasripoo, F.: Advanced seals for industial turbine applicaitons: dynamic seal development. J. Propul. Power **18**, 1260–1265 (2002)
18. Morell, P.R., Patel, M., Skinner, A.R.: Accelerated thermal ageing studies on nitrile rubber O-rings. Polym. Test. **22**(6), 651–656 (2003)
19. Chivers, T.C., Geroge, A.F.: EPDM and fluorocarbon seal materials: a comparison of performance for nuclear fuel transport flasks. In: 14th International Symposium on the Packaging and Transportation of Radioactive Materials. Berlin, (2004)
20. Kommling, M.J.: Influence of ageing on sealability of elastomeric O-rings. In: Macromol Symposium (pp. 1–10). Wiley, Weinheim, (2017)
21. Liao, B., Sun, B., Yan, M., et al.: Time-variant reliability analysis for rubber O-ring seal considering both material degradation and random load. Materials **10**, 1211 (2017)
22. Zhang, J., Xie, J.: Investigation of static and dynamic seal performances of a rubber O-ring. J. Tribol. **140**, 042202 (2018)
23. Pearl, D.R.: O-ring seals in the design of hydraulic mechanism. SAI annual meeting. Jan 1947.
24. Parker, O.: Parker O-ring Handbook. Parker Hannifin Corporation, Cleveland (2018)
25. Thomas, A.G.: Factors influencing the strength of rubbers. J. Polym. Sci. **48**, 145–157 (1974)
26. Pornprasit, R., Pornprasit, P., et al.: Determination of the mechanical properties of rubber by FT-NIR. J. Spect. 1–7 (2016)
27. Aji, H.S., Soepangkat, B.O.P., Santosa, B., Norcahyo, R.: Multi objective optimization of vulcanization process parameters for reducing quality loss cost based on BPNN-PSO method. In: AIP Conference Proceedings, vol. 2114, p. 020012, (2019)
28. Schulze, D., Fengler, P., Stark, W.: The determination of ozone concentration for ozone resistance tests of elastomers. KGK Kaut. Gummi Kunstst. **64**, 15–19 (2011)
29. Kulkarni, S.D., Manjunatha, C.U.: Effect of manufacturing process parameters on the tear strength and compression set of polyvinyl-nitrile rubber for sealing applications. Eur. Chem. Bull. **12**, 245–258 (2023). https://doi.org/10.31838/ecb/2023.12.s1.027
30. Kulkarni, S.D., Manjunatha, B., Chandrasekhar, U., Siddesh, G.K., Lenin, H., Arul, S.J.: Effect of curing temperature and time on mechanical properties of vinyl polymer material for sealing applications in industry using machine learning techniques. Adv. Polym. Technol. (2023). https://doi.org/10.1155/2023/9964610
31. Pornprasit, R., Pornprasit, P., Boonma, P., Natwichai, J.: Determination of the mechanical properties of rubber by FT-NIR. J. Spect. **4024783**, 7 (2016)
32. Clarke, J., Clarke, B., Freakley, P.K., Sutherland, I.: Compatibilising effect of carbon black on morphology of NRNBR blends. Plast. Rubber Compos. Process. Appl. **30**(1), 39–44 (2001)

33. Chough, S.-H., Chang, D.-H.: Kinetics of sulfur vulcanization of NR, BR, SBR, and their blends using a rheometer and DSC. J. Appl. Polym. Sci. **61**(3), 449–454 (1996)

34. White, R.: Fractography of Rubbery Materials, p. 33. Elsevier Science Publishers, LTD, London (1991)

35. Jenkins, R.C., Meherc, J.W., Linn, J.V.: Paper No. 184th Fall Technical Meeting, Rubber Division, ACS, (1963)

36. Vasudev, H., Prakash, C.: Surface engineering and performance of biomaterials: editorial. J. Electrochem. Sci. Eng. **13**(1), 1–3 (2023). https://doi.org/10.5599/jese.1698

37. Poojari, M., Hanumanthappa, H., et al.: Computational modelling for the manufacturing of solar-powered multifunctional agricultural robot. Int. J. Inter. Des. Manuf. (2023). https://doi.org/10.1007/s12008-023-01291-y

38. Manjunatha, C., et al.: Influence of microstructural characteristics on wear and corrosion behaviour of Si3N4 reinforced Al2219 composites. Adv. Mater. Sci. Eng. **2023**, 1120569 (2023). https://doi.org/10.1155/2023/1120569

39. Sharanabasva, H., et al.: Characterization and wear behavior of NiCrMoSi microwave cladding. J. Mater. Eng. Perform. (2023). https://doi.org/10.1007/s11665-023-07998-z

40. Mehta, A., Singh, G.: Consequences of hydroxyapatite doping using plasma spray to implant biomaterials: review paper. J. Electrochem. Sci. Eng. **13**(1), 5–23 (2023). https://doi.org/10.5599/jese.1614

41. Nithin, H.S., Nishchitha, K.M., Pradeep, D.G., Durga Prasad, C., et al.: Comparative analysis of CoCrAlY coatings at high temperature oxidation behavior using different reinforcement composition profiles. Weld. World **67**, 585–592 (2023). https://doi.org/10.1007/s40194-022-01405-2

42. Sharanabasva, H., et al.: Effect of Mo and SiC reinforced NiCr microwave cladding on microstructure, mechanical and wear properties. J. Instit. Eng. (2023). https://doi.org/10.1007/s40033-022-00445-8

43. Naveen, D.C., et al.: Effects of polypropylene waste addition as coarse aggregate in concrete: experimental characterization and statistical analysis. Adv. Mater. Sci. Eng. (2022). https://doi.org/10.1155/2022/7886722

44. Gowda, V., et al.: High-temperature tribological studies on hot forged Al6061- Tib2 in-situ composites. J. Bio Tribo-Corros. **8**, 101 (2022). https://doi.org/10.1007/s40735-022-00699-5

45. Madhusudana Reddy, G., et al.: Elevated temperature erosion performance of plasma sprayed NiCrAlY/TiO2 coating on MDN 420 steel substrate. Surf. Topogr. Metrol. Proper. **10**, 025010 (2022). https://doi.org/10.1088/2051-672X/ac6a6e

46. Singh, J., Singh, J.P., Kumar, S., Gill, H.S.: Short review on hydroxyapatite powder coating for SS 316L: review paper. J. Electrochem. Sci. Eng. **13**(1), 25–39 (2023). https://doi.org/10.5599/jese.1611

47. Prashar, G., Vasudev, H.: Understanding cold spray technology for hydroxyapatite deposition: review paper. J. Electrochem. Sci. Eng. **13**(1), 41–62 (2023). https://doi.org/10.5599/jese.1424

48. Madhusudana Reddy, G., et al.: Investigation of thermally sprayed NiCrAlY/TiO2 and NiCrAlY/Cr2O3/YSZ cermet composite coatings on titanium alloys. Eng. Res. Express **4**, 025049 (2022). https://doi.org/10.1088/2631-8695/ac7946

49. Madhusudana Reddy, G., et al.: High temperature oxidation behavior of plasma sprayed NiCrAlY/TiO2 & NiCrAlY /Cr2O3/YSZ coatings on titanium alloy. Weld. World (2022). https://doi.org/10.1007/s40194-022-01268-7

50. Naik, T., et al.: Effect of laser post treatment on microstructural and sliding wear behavior of HVOF sprayed NiCrC and NiCrSi coatings. Surf. Rev. Lett. **29**(1), 225000 (2022). https://doi.org/10.1142/S0218625X2250007X

51. Madhusudana Reddy, G., et al.: High temperature oxidation studies of plasma sprayed NiCrAlY/TiO2 & NiCrAlY/Cr2O3/YSZ cermet composite coatings on MDN-420 special steel alloy. Metallogr. Microst. Anal. **10**, 642–651 (2021). https://doi.org/10.1007/s13632-021-00784-0

52. Mathapati, M., et al.: A review on fly ash utilization. Mater. Today Proc. Sci. **50**, 1535–1540 (2022). https://doi.org/10.1016/j.matpr.2021.09.106

53. Dinesh, R., et al.: Feasibility study on MoCoCrSi/ WC-Co cladding developed on austenitic stainless steel using microwave hybrid heating. J. Mines Metals Fuels (2021). https://doi.org/10.18311/jmmf/2021/30113

54. Durga Prasad, C., Lingappa, S., Sharnappa Joladarashi, M.R., Ramesh, S.B.: Characterization and sliding wear behavior of CoMoCrSi+flyash composite cladding processed by microwave irradiation. Mater. Today Proc **46**, 2387–2391 (2021). https://doi.org/10.1016/j.matpr.2021.01.156

55. Madhu, G., et al.: Evaluation of hot corrosion behavior of HVOF thermally sprayed Cr3C2 -35NiCr coating on SS 304 boiler tube steel. Am. Inst. Phys. **2316**, 030014 (2021). https://doi.org/10.1063/5.0038279

56. Reddy, M.S., Durga Prasad, C., Pradeep Patil, M.R., Ramesh, N.R.: Hot corrosion behavior of plasma sprayed NiCrAlY/TiO2 and NiCrAlY/Cr2O3/YSZ cermets coatings on alloy steel. Surf. Interf. Sci. **22**, 100810 (2021). https://doi.org/10.1016/j.surfin.2020.100810

57. Singh, J., Singh, S., Gill, R.: Applications of biopolymer coatings in biomedical engineering: review paper. J. Electrochem. Sci. Eng. **13**(1), 63–81 (2022). https://doi.org/10.5599/jese.1460

58. Singh, J., Singh, S., Verma, A.: Artificial intelligence in use of ZrO2 material in biomedical science: review paper. J. Electrochem. Sci. Eng. **13**(1), 83–97 (2022). https://doi.org/10.5599/jese.1498

59. Singh, G., Singh, R., Gul, J.: Machinability behavior of human implant materials: original scientific paper. J. Electrochem. Sci. Eng. **13**(1), 99–114 (2022). https://doi.org/10.5599/jese.1514

60. Durga Prasad, C., et al.: Microstructure and tribological resistance of flame sprayed CoMoCrSi/WC-CrC-Ni and CoMoCrSi/WC-12Co composite coatings remelted by microwave hybrid heating. J. Bio Tribo-Corros. **6**, 124 (2020). https://doi.org/10.1007/s40735-020-00421-3

61. C. Durga Prasad, Sharnappa Joladarashi, M. R Ramesh, "Comparative Investigation of HVOF and Flame Sprayed CoMoCrSi Coating". American Institute of Physics, 2247, 050004 (2020) https://doi.org/10.1063/5.0003883

62. C. Durga Prasad, Akhil Jerri, M. R. Ramesh, "Characterization and Sliding Wear Behavior of Iron Based Metallic Coating Deposited by HVOF Process on Low Carbon Steel Substrate". Journal of Bio and Tribo-Corrosion, Springer, 6, 69 (2020). https://doi.org/10.1007/s40735-020-00366-7

63. C. Durga Prasad, Sharnappa Joladarashi, M. R. Ramesh, M. S. Srinath, B. H. Channabasappa. "Comparison of High Temperature Wear Behavior of Microwave Assisted HVOF Sprayed CoMoCrSi-WC-CrC-Ni/WC-12Co Composite Coatings". Silicon, Springer, 12, pp 3027–3045 (2020) 1–19 https://doi.org/10.1007/s12633-020-00398-1

64. Abdulaah, H.A., Al-Ghaban, A.M., Anaee, R.A., Khadom, A.A., Kadhim, M.M.: Cerium-tricalcium phosphate coating for 316L stainless steel in simulated human fluid: experimental, biological, theoretical, and electrochemical investigations: original scientific paper. J. Electrochem. Sci. Eng. **13**(1), 115–126 (2022). https://doi.org/10.5599/jese.1257

65. Jawade, S., Kakandikar, G.: Relationship modelling for surface finish for laser-based additive manufacturing: original scientific paper. J. Electrochem. Sci. Eng. **13**(1), 127–135 (2023). https://doi.org/10.5599/jese.1286

66. Durga Prasad, C., Sharnappa Joladarashi, M.R., Ramesh, M.S., Srinath, B., Channabasappa., H.: Effect of microwave heating on microstructure and elevated temperature adhesive wear behavior of

HVOF deposited CoMoCrSi-Cr$_3$C$_2$ composite coating. Surf. Coat. Technol. **374**, 291–304 (2019). https://doi.org/10.1016/j.surfcoat.2019.05.056

67. Durga Prasad, C., Sharnappa Joladarashi, M.R., Ramesh, M.S., Srinath, B., Channabasappa, H.: Development and sliding wear behavior of Co-Mo-Cr-Si cladding through microwave heating. SILICON **11**, 2975–2986 (2019). https://doi.org/10.1007/s12633-019-0084-5

68. Durga Prasad, C., Sharnappa Joladarashi, M.R., Ramesh, M.S., Srinath, B., Channabasappa., H.: Microstructure and tribological behavior of flame sprayed and microwave fused CoMoCrSi/CoMoCrSi-Cr$_3$C$_2$ Coatings. Mater. Res. Express **6**, 026512 (2019). https://doi.org/10.1088/2053-1591/aaebd9

69. Sandhu, K., Singh, G., Singh, S., Kumar, R., Prakash, C., Ramakrishna, S., Królczyk, G., Pruncu, C.I.: Surface characteristics of machined polystyrene with 3D printed thermoplastic tool. Materials. **13**, 2729 (2020)

70. Antil, P., Kumar Antil, S., Prakash, C., Krolczyk, G., Pruncu, C.: Multi-objective optimization of drilling parameters for orthopaedic implants. Measur. Contr. **53**, 1902–1910 (2020)

71. Kumar, A., Grover, N., Manna, A., Chohan, J.S., Kumar, R., Singh, S., Prakash, C., Pruncu, C.I.: Investigating the influence of WEDM process parameters in machining of hybrid aluminum composites. Adv. Compos. Lett. **29**, 2633366X20963137 (2020)

72. Durga Prasad, C., Sharnappa Joladarashi, M.R., Ramesh, M.S., Srinath, B., Channabasappa, H.: Influence of microwave hybrid heating on the sliding wear behaviour of HVOF sprayed CoMoCrSi coating. Mater. Res. Express **5**, 086519 (2018). https://doi.org/10.1088/2053-1591/aad44e

73. Durga Prasad, C., Sharnappa Joladarashi, M.R., Ramesh, A.S.: High temperature gradient cobalt based clad developed using microwave hybrid heating. Am. Inst. Phys. **1943**, 020111 (2018). https://doi.org/10.1063/1.5029687

74. Girisha, K.G., Sreenivas Rao, K.V., Durga Prasad, C.: Slurry erosion resistance of martenistic stainless steel with plasma sprayed Al$_2$O$_3$-40%TiO$_2$ coatings. Mater. Today Proc. **5**, 7388–7393 (2018). https://doi.org/10.1016/j.matpr.2017.11.409

75. Girisha, K.G., Durga Prasad, C., Anil, K.C., Sreenivas Rao, K.V.: Dry sliding wear behaviour of Al$_2$O$_3$ coatings for AISI 410 grade stainless steel. Appl. Mech. Mater. **766–767**, 585–589 (2015). https://doi.org/10.4028/www.scientific.net/AMM.766-767.585

76. Girisha, K.G., Rakesh, R., Durga Prasad, C., Sreenivas Rao, K.V.: Development of corrosion resistance coating for AISI 410 grade steel. Appl. Mech. Mater. **813–814**, 135–139 (2015). https://doi.org/10.4028/www.scientific.net/AMM.813-814.135

77. Kundu, S., Thakur, L.: Microhardness and biological behavior of AZ91D-nHAp surface composite for bio-implants: original scientific paper. J. Electrochem. Sci. Eng. **13**(1), 137–147 (2022). https://doi.org/10.5599/jese.1316

78. Channi, A.S., Bains, H.S., Grewal, J.S., Chidambranathan, V.S., Kumar, R.: Tool wear rate during electrical discharge machining for aluminium metal matrix composite prepared by squeeze casting: a prospect as a biomaterial: original scientific paper. J. Electrochem. Sci. Eng. **13**(1), 149–162 (2022). https://doi.org/10.5599/jese.1391

79. Yedida, V.V.S., Vasudev, H.: Mechanical and microstructural characterization of YSZ/Al$_2$O$_3$/CeO$_2$ plasma sprayed coatings: original scientific paper. J. Electrochem. Sci. Eng. **13**, 163–172 (2022). https://doi.org/10.5599/jese.1431

80. Singh, J.P., Sharma, Y.: Corrosion cracking in Mg alloys based bioimplants: review paper. J. Electrochem. Sci. Eng. **13**(1), 193–214 (2023). https://doi.org/10.5599/jese.1636

81. Raghavan, V., Rajasekaran, S.J.: Corrigendum to Palmyra palm flower biomass-derived activated porous carbon and its application as a supercapacitor electrode: corrigendum. J. Electrochem. Sci. Eng. **13**(1), 215 (2023). https://doi.org/10.5599/jese.1658

82. Akande, I.G., Fayomi, O.S.I., Akpan, B.J., Aogo, O.A., Onwordi, P.N.: Exploration of the effect of Zn-MgO-UPP coating on hardness, corrosion resistance and microstructure properties of mild steel: original scientific paper. J. Electrochem. Sci. Eng. **12**(5), 829–840 (2022). https://doi.org/10.5599/jese.1311

83. Singh, M., Vasudev, H., Singh, M.: Surface protection of SS-316L with boron nitride based thin films using radio frequency magnetron sputtering technique: original scientific paper. J. Electrochem. Sci. Eng. **12**(5), 851–863 (2022). https://doi.org/10.5599/jese.1247

84. Prakash, C., Nagarajan, R.: Outburst susceptibility assessment of moraine-dammed lakes in Western Himalaya using an analytic hierarchy process. Earth Surf. Proc. Land. **42**, 2306–2321 (2017)

85. Singh, S., Prakash, C., Antil, P., Singh, R., Królczyk, G., Pruncu, C.I.: Dimensionless analysis for investigating the quality characteristics of aluminium matrix composites prepared through fused deposition modelling assisted investment casting. Materials. **12**, 1907 (2019)

86. Singh, S., Singh, N., Gupta, M., Prakash, C., Singh, R.: Mechanical feasibility of ABS/HIPS-based multi-material structures primed by low-cost polymer printer. Rapid Prototyp. J. **25**, 152–161 (2019)

87. Kumar, R., Ranjan, N., Kumar, V., Kumar, R., Chohan, J.S., Yadav, A., Sharma, S., Prakash, C., Singh, S., Li, C.: Characterization of friction stir-welded polylactic acid/aluminum composite primed through fused filament fabrication. J. Mater. Eng. Perfor. **2021**, 1–19 (2021)

88. Singh, H., Singh, S., Prakash, C.: Current trends in biomaterials and bio-manufacturing. Biomanufacturing **2019**, 1–34 (2019)

89. Jin, S.Y., Pramanik, A., Basak, A.K., Prakash, C., Shankar, S., Debnath, S.: Burr formation and its treatments—a review. Int. J. Adv. Manuf. Technol. **107**, 2189–2210 (2020)

90. Prakash, C., Singh, S., Ramakrishna, S., Królczyk, G., Le, C.H.: Microwave sintering of porous Ti–Nb-HA composite with high strength and enhanced bioactivity for implant applications. J. Alloy. Compd. **824**, 153774 (2020)

91. Uddin, M., Basak, A., Pramanik, A., Singh, S., Krolczyk, G.M., Prakash, C.: Evaluating hole quality in drilling of Al 6061 alloys. Materials. **11**, 2443 (2018)

92. Pandey, A., Singh, G., Singh, S., Jha, K., Prakash, C.: 3D printed biodegradable functional temperature-stimuli shape memory polymer for customized scaffoldings. J. Mech. Behav. Biomed. Mater. **108**, 103781 (2020)